Compressive imaging of subwavelength structures: periodic rough surfaces

Albert Fannjiang* and Hsiao-Chieh Tseng

Department of Mathematics, University of California, Davis, California 95616-8633, USA
**Corresponding author: fannjiang@math.ucdavis.edu*

Received September 1, 2011; accepted November 12, 2011;
posted November 22, 2011 (Doc. ID 153721); published March 27, 2012

A compressed sensing scheme for near-field imaging of corrugations of relative sparse Fourier components is proposed. The scheme employs random sparse measurement of near field to recover the angular spectrum of the scattered field. Surprisingly, it can be shown heuristically and numerically that under the Rayleigh hypothesis the angular spectrum is compressible and amenable to compressed sensing techniques. Iteration schemes are developed for recovering the surface profile from the angular spectrum. The proposed nonlinear least squares in the Fourier basis produces accurate reconstructions even when the Rayleigh hypothesis is known to be false.

1. INTRODUCTION

Rough surface scattering is of fundamental interest in optics, radiowave propagation, and acoustics [1–8] and forms the basis of near-field imaging, which is the operation principle behind such instruments as scanning near-field optical microscopy [9–12] and near-field acoustic microscopy [13]. Near-field imaging is a microscopic technique that breaks the diffraction limit by exploiting the properties of evanescent waves. The signal is collected by placing the detector in a distance much smaller than wavelength λ to the specimen surface. An image of the surface is obtained by mechanically moving the probe in a raster scan of the specimen, line by line, and recording the probe-surface interaction as a function of position. This leads to long scan times for large sample areas or high resolution imaging.

Typically near-field imaging is analyzed by assuming a continuum or dense set of data points [14–16]. In the present work, we focus on the setting of *sparse*, *discrete* measurement of near field from the perspective of compressed sensing theory. This is an extension of the work [17] on potential scattering to the case of rough surface scattering. Surface scattering involves the geometry (i.e., topography) of scatterer and is fully nonlinear and more challenging than potential scattering.

Consider the scattering problem for a corrugation profile described by the function $z = h(x)$, Fig. 1. For simplicity of presentation, we focus on the case of two-dimensional scalar wave with the Dirichlet boundary condition. The total field u^{tot} satisfies

$$\begin{aligned} \Delta u^{\text{tot}} + k^2 u^{\text{tot}} &= 0 \quad \text{in} \quad \Omega \subset \mathbb{R}^2, \quad k > 0 \\ u^{\text{tot}} &= 0 \qquad\quad \text{on} \quad \partial\Omega, \end{aligned}$$

where

$$\Omega = \{r = (x, z) \in \mathbb{R}^2 : z > h(x)\}, \qquad h \in C(\mathbb{R}) \cap L^\infty(\mathbb{R}).$$

The total field models the sound pressure field or electric field in the TE mode. The Dirichlet boundary condition corresponds to the sound-soft boundary condition in acoustics and the perfectly conducting boundary condition in electromagnetism. Our approach can easily be extended to the three-dimensional case as well as to the Neumann boundary condition, corresponding to acoustically hard obstacles and the insulated boundary condition.

As usual in a scattering problem, we write $u^{\text{tot}} = u^{\text{inc}} + u$ where both the scattered wave u and the incident wave u^{inc} satisfy the Helmholtz equation. The Dirichlet condition becomes $u = -u^{\text{inc}}$ on $\partial\Omega$.

In this paper, we consider the case of periodic surfaces that include diffraction gratings, an important class of optical elements. We also assume that we have the knowledge of the scattered *field*, which can be obtained by using, for instance, the techniques of near-field phase-shifting interferometry [18]. The main focus of the present work is on the *fully nonlinear* inverse scattering of rough surfaces and the compression of measurements with compressed sensing techniques [19,20].

Let L be the period of h and u^{inc} the plane incident wave

$$u^{\text{inc}}(\boldsymbol{r}) = e^{ik\hat{\boldsymbol{d}}\cdot\boldsymbol{r}} = e^{ik(x\cos\theta - z\sin\theta)},$$
$$\hat{\boldsymbol{d}} = (\cos\theta, -\sin\theta), \qquad 0 < \theta < \pi.$$

Observe that on the boundary $z = h(x)$

$$u(x + L, h(x)) = -e^{ik\left((x+L)\cos\theta - h(x)\sin\theta\right)} = e^{ikL\cos\theta} u(x, h(x)).$$

Hence we look for the $(L, k\cos\theta)$-quasiperiodic (or Floquet periodic) solution satisfying

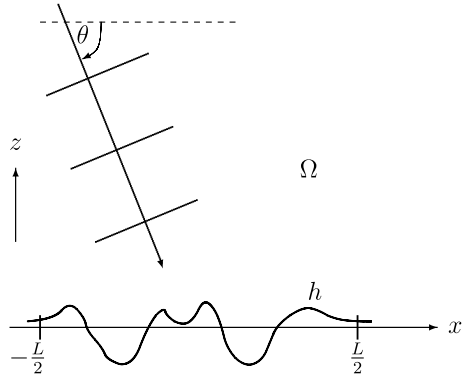

Fig. 1. Plane wave incidence upon a rough surface.

$$u(x+nL,z)=e^{inLk\cos\theta}u(x,z)$$
$$\text{for all } (x,z)\in\Omega,\qquad n\in\mathbb{Z}.$$

In particular, if $\theta=\pi/2$, then u is L periodic. To fix the idea, we set $L=2\pi$.

2. RADIATION CONDITION AND RAYLEIGH HYPOTHESIS

The existence and uniqueness can be proved under the quasiperiodicity and the radiation conditions on the solution u [21]. The well-posedness for general nonperiodic rough surfaces is given in [22].

Scattering and imaging of shallow corrugations have been treated by assuming the Kirchhoff approximation [7], the Rytov approximation [4], or the Born approximation [23]. Instead our approach is based on the Rayleigh hypothesis, which is discussed below.

For $x\in[-\pi,\pi)$, $z>\sup h\triangleq h_{\max}$, we write the scattered field as the Fourier series

$$u(x,z)=\sum_{n\in\mathbb{Z}}u_n(z)e^{i(n+k\cos\theta)x}=\sum_{n\in\mathbb{Z}}u_n(z)e^{ik\alpha_n x}$$

with

$$\alpha_n=\frac{n}{k}+\cos\theta, \tag{1}$$

where u_n satisfies

$$\ddot{u}_n+k^2(1-\alpha_n^2)u_n=0. \tag{2}$$

Solving Eq. (2) and imposing the boundedness of u_n at $z=\infty$, we obtain the general solution as

$$\begin{aligned}u(x,z)=&\sum_{|\alpha_n|\le 1}a_n e^{ik(\alpha_n x-\beta_n z)} &&\text{(incoming waves)}\\&+\sum_{|\alpha_n|\le 1}b_n e^{ik(\alpha_n x+\beta_n z)} &&\text{(outgoing waves)}\\&+\sum_{|\alpha_n|>1}c_n e^{ik(\alpha_n x+\beta_n z)} &&\text{(evanescent waves)},\end{aligned} \tag{3}$$

where β_n is given by

$$\beta_n=\begin{cases}\sqrt{1-\alpha_n^2}, & |\alpha_n|\le 1\\ i\sqrt{\alpha_n^2-1}, & |\alpha_n|>1.\end{cases} \tag{4}$$

The Rayleigh *radiation* condition for the region above the grooves $z>h_{\max}$ amounts to dropping the incoming waves in Eq. (3):

$$u(x,z)=\sum_{n\in\mathbb{Z}}u_n e^{ik(\alpha_n x+\beta_n z)},\qquad z>h_{\max}. \tag{5}$$

However, in the region inside the grooves $z<h_{\max}$ multiple scattering may occur and Eq. (5) may not represent the true scattered wave in this region. For shallow corrugations, however, Eq. (5) should hold in the grooves, and this is the Rayleigh hypothesis. For instance, the Rayleigh hypothesis holds for the sinusoidal profile $h(x)=b\sin(ax)$ with $|ab|<0.448$ [5,24,25]. On the other hand, for a general periodic surface the validity of the Rayleigh hypothesis may be difficult to assess [26]. The failure of the Rayleigh hypothesis manifests in the breaking down of the analyticity of (5) inside grooves and is attributable to the roughness instead of the subwavelength modes of the profile. For example, the preceding sinusoidal profile does not contain any subwavelength mode if $|a|<k$ but violates the Rayleigh hypothesis if $|ab|$, a metric of roughness, is above a certain threshold. The validity of the Rayleigh hypothesis is often implicitly assumed in the literature (e.g., [8]).

3. INVERSE SCATTERING FORMULATION

The goal of inverse scattering is to reconstruct $h(x)$ by transmitting incident wave u^{inc} and measuring the scattered field u at certain sampling locations. To resolve subwavelength structure that is hidden in the evanescent waves, the measurement should be carried out in the near field.

Because of the quasiperiodicity, we may consider the scattered field u in the union of

$$\Omega_\Gamma\triangleq\{(x,z)\in\Omega, x\in[-\pi,\pi)\}$$

and

$$\Gamma\triangleq\{(x,z)\in\partial\Omega: x\in[-\pi,\pi)\}.$$

For $z>h(x)$ we have the outgoing scattered wave representation Eq. (5) with [27]

$$u_n=\frac{i}{4\pi k\beta_n}\int_{-\pi}^{\pi}e^{-ik\left(\alpha_n x'+\beta_n h(x')\right)}\left(-\frac{\partial u^{\text{tot}}(\boldsymbol{r}')}{\partial\nu'}\bigg|_{\boldsymbol{r}'\in\Gamma}\right)\sqrt{1+\dot{h}^2(x')}\,dx'. \tag{6}$$

To ensure $\beta_n\neq 0$ in Eq. (6), we assume that $|\alpha_n|\neq 1$, i.e.,

$$\left|\cos\theta+\frac{n}{k}\right|\neq 1,\qquad n\in\mathbb{Z} \tag{7}$$

to avoid all grazing modes. This is a constraint on the choice of wavenumber and the incidence angle. In the case of normal incidence $\theta=\pi/2$, Eq. (7) means that the wavenumber k is not an integer.

A key assumption for our approach is that h has a *small number* of significant Fourier coefficients, namely, the Fourier coefficients are sparse or compressible. Writing $h(x) = \sum_{n\in\mathbb{Z}} \hat{h}_n e^{inx}$, we say that $\hat{\boldsymbol{h}} = \{\hat{h}_n\}$ is s sparse if $\|\hat{\boldsymbol{h}}\|_0$, the number of nonzero elements of $\hat{\boldsymbol{h}}$, is less than or equal to s. Note that $\hat{h}^*_{-n} = \hat{h}_n$ since h is real valued. Without loss of generality, we assume that $\hat{h}_0 = 0$.

The sparsity of $\hat{\boldsymbol{h}}$ surprisingly yields compressibility of the scattering amplitude u_n, which can be used to compress the measurements and be amenable to the treatment of compressive sensing techniques.

Let $(x_j, z_0), j = 1, 2, \ldots, m$, be the sensor locations for measuring the scattered field where $z_0 > h_{\max}$ is fixed and x_j are randomly and independently chosen from $[-\pi, \pi)$ according to the *uniform* distribution.

In view of the identity

$$u(x_j, z_0)e^{-ik\cos\theta x_j} = \sum_{n\in\mathbb{Z}} e^{inx_j} u_n e^{ik\beta_n z_0}$$

from Eq. (5), let us consider the following inverse problem $Y = \mathbf{A}X$, with entries

$$X_n = u_n e^{ik\beta_n z_0}\sqrt{m}, \tag{8}$$

$$Y_j = u(x_j, z_0)e^{-ikx_j\cos\theta}, \tag{9}$$

$$\mathbf{A} = [A_{j,n}] = \frac{1}{\sqrt{m}} e^{inx_j}, \tag{10}$$

where n is restricted to a finite but sufficiently large interval ranged from $-N/2$ to $N/2 - 1$. A compressive measurement means the number of data m is significantly smaller than the number of grid points N, giving rise to a highly underdetermined system Eqs. (8)–(10).

4. COMPRESSIVE SENSING

The main thrust of compressed sensing (CS) [19,20] is to convert the noisy underdetermined system

$$Y = \mathbf{A}X + E \tag{11}$$

into the L^1-based optimization problem

$$\min \|X\|_1 \text{ subject to} \|Y - \mathbf{A}X\|_2 \le \epsilon \triangleq \|E\|_2, \tag{12}$$

where E is the external noise vector. Equation (12) is called the basis pursuit (BP) [28]. In addition to quadratic programming, many iterative and greedy algorithms are available for solving the system Eq. (11).

Let us first review a basic notion in CS, which provides a performance guarantee for BP. We say a matrix $\mathbf{A} \in \mathbb{C}^{m\times N}$ satisfies the restricted isometry property (RIP) if

$$(1-\delta)\|Z\|_2^2 \le \|\mathbf{A}Z\|_2^2 \le (1+\delta)\|Z\|_2^2, \qquad \delta \in (0,1), \tag{13}$$

holds for all s-sparse $Z \in \mathbb{C}^N$. The smallest constant satisfying Eq. (13) is called the restricted isometry constant of order s and is denoted by δ_s.

The following theorem says that the random Fourier matrix satisfies RIP if m is sufficiently large [29].

Theorem 1. Let $\xi_j \in [0, 1]$, $j = 1, 2, \ldots, m$, be independent uniform random variables. If

$$\frac{m}{\ln m} \ge C\delta^{-2} s \ln^2 s \ln N \ln\frac{1}{\eta}, \qquad \eta \in (0,1)$$

for some universal constant C and sparsity level s, then the restricted isometry constant of the random Fourier measurement matrix with

$$A_{nj} = \frac{1}{\sqrt{m}} e^{2\pi i n\xi_j}, \qquad n = -N/2, \ldots, N/2 - 1, \tag{14}$$

satisfies $\delta_s \le \delta$ with probability at least $1 - \eta$.

Denote X_s to be the best s-term approximation of the solution X, and let $\tilde{X}$ be the solution of BP Eq. (12). Note that X_s consists of the s largest components, in magnitude, of X.

Theorem 2 [30]. Let $\mathbf{A}$ satisfy the RIP with

$$\delta_{2s} < \sqrt{2} - 1$$

and $\tilde{X}$ be the solution to BP. Then

$$\|\tilde{X} - X\|_2 \le C_0 \frac{1}{\sqrt{s}}\|X_s - X\|_1 + C_1\epsilon, \qquad \|\tilde{X} - X\|_1 \le C_0\|X_s - X\|_1 + C_1\epsilon$$

for some constants C_0, C_1 independent of X.

Once the estimate $\tilde{X}$ is obtained from BP, we reconstruct u_n by

$$\tilde{u}_n = \frac{1}{\sqrt{m}} e^{-ik\beta_n z_0}\tilde{X}_n. \tag{15}$$

The problem with Eq. (15) is that the evanescent modes yield the exponentially large factor $e^{-ik\beta_n z_0}$ if

$$|\alpha_n| = \left|\cos\theta + \frac{n}{k}\right| \gg 1. \tag{16}$$

This can magnify the error in $\tilde{X}_n$ and produce an undesirable result in $\tilde{u}_n$. This observation also shows that X may be much more compressible (i.e., faster decaying components) than $\{u_n\}$.

A simple remedy would be to apply a hard thresholding by restricting the identity Eq. (15) up to n_0 sufficiently small and setting the rest of $\tilde{u}_n$ zero for $|n| > n_0$. Let us now give a rough estimate for the number of modes that should be preserved by the hard thresholding rule.

We define the stably recoverable evanescent modes to be those modes satisfying Eq. (16) and

$$k|\beta_n|z_0 \le C_e$$

for some constant C_e (in [17], $C_e = 2\pi$). On the other hand,

$$\beta_n = \sqrt{\cos^2\theta + 2\frac{n}{k}\cos\theta + \frac{n^2}{k^2} - 1} \ge \frac{|n|}{k} - 1.$$

Hence the stably recoverable modes necessarily satisfy

$$k\left(\frac{|n|}{k}-1\right)z_0 \le k|\beta_n|z_0 \le C_e$$

or equivalently

$$|n| \le n_0 \triangleq \frac{C_e}{z_0}+k, \tag{17}$$

which is a rough characterization of the stably recoverable (evanescent) modes. We see that n_0 increases as k increases or z_0 decreases.

Summing up the previous analysis, we conclude the recoverability of the scattering amplitude $\{u_n\}$ by the following theorem.

Theorem 3. Let $z_0 > h_{\max}$ be fixed and let x_j, $j=1,2,\dots,m$, be independent, identically distributed (i.i.d.) uniform random variables in $[-\pi,\pi)$. Let $n_0 = \frac{C_e}{z_0}+k$ for some positive constant $C_e > 0$. Let $\tilde{X}, X_s$ be the BP solution and the best s-term approximated solution of the system Eq. (11), respectively, and assume

$$\frac{m}{\ln m} > \frac{C}{(\sqrt{2}-1)^2} s \ln^2 s \ \ln N \ \ln\frac{1}{\eta}$$

for some absolute constant C and any $\eta \in (0,1)$. Let $\boldsymbol{u} = (u_{-n_0},\dots,u_{n_0})$, $\tilde{\boldsymbol{u}} = (\tilde{u}_{-n_0},\dots,\tilde{u}_{n_0})$, where $\tilde{u}_n$ is given by Eq. (15). Then the reconstruction error satisfies

$$\|\tilde{\boldsymbol{u}}-\boldsymbol{u}\|_2 \le \frac{e^{C_e}}{\sqrt{m}}\left(C_0\frac{1}{\sqrt{s}}\|X_s-X\|_1 + C_1\epsilon\right) \tag{18}$$

for some absolute constants C_0, C_1 with probability at least $1-\eta$.

Proof. With $x_j = 2\pi(\xi_j - \frac{1}{2})$, the sensing matrix (10) becomes

$$[A_{j,n}] = \frac{1}{\sqrt{m}}e^{in2\pi(\xi_j-\frac{1}{2})} = \frac{1}{\sqrt{m}}e^{2\pi i n\xi_j}(-1)^n.$$

By combining the factor $(-1)^n$ into X_n and writing $W_n = (-1)^n X_n$, $n=-N/2,\dots,N/2-1$, we have $\|\tilde{W}-W\|_2 = \|\tilde{X}-X\|_2$, $\|W_s-W\|_1 = \|X_s-X\|_1$, where $\tilde{W}$ and W_s are defined in the same manner.

Hence with i.i.d. uniform random variables x_j, $j=1,2,\dots,m$, in $[0,2\pi)$, the matrix $\mathbf{A}$ defined in Eq. (10) satisfies the same reconstruction error bound as the random Fourier measurement Eq. (14) with i.i.d. uniform random variables ξ_j on $[0,1)$. By Theorems 1 and 2, we have the estimate

$$\|\tilde{X}-X\|_2 \le C_0\frac{1}{\sqrt{s}}\|X_s-X\|_1 + C_1\epsilon$$

for some constants C_0, C_1 with probability at least $1-\eta$. On the other hand,

$$\|\tilde{X}-X\|_2^2 = \sum_{n=-n_0}^{n_0}\left|\tilde{u}_n e^{ik\beta_n z_0}\sqrt{m} - u_n e^{ik\beta_n z_0}\sqrt{m}\right|^2 + \sum_{n\in\Lambda}\left|\tilde{X}_n - X_n\right|^2,$$

where $\Lambda \triangleq \{-N/2,\dots,-n_0+1,n_0+1,N/2-1\}$. Moreover, for $|n| \le n_0$ we have $0 < |e^{-C_e}| \le |e^{ik\beta_n z_0}| \le 1$, which gives

$$\|\tilde{X}-X\|_2^2 \ge m|e^{-C_e}|^2\sum_{n=-n_0}^{n_0}|\tilde{u}_n-u_n|^2 + 0 = \frac{m}{e^{2C_e}}\|\tilde{\boldsymbol{u}}-\boldsymbol{u}\|_2^2,$$

where $\boldsymbol{u} = (u_{-n_0},\dots,u_{n_0})$ and $\tilde{\boldsymbol{u}} = (\tilde{u}_{-n_0},\dots,\tilde{u}_{n_0})$. Combining these inequalities, we have the bound

$$\|\tilde{\boldsymbol{u}}-\boldsymbol{u}\|_2 \le \frac{e^{C_e}}{\sqrt{m}}\left(C_0\frac{1}{\sqrt{s}}\|X_s-X\|_1 + C_1\epsilon\right)$$

for some constants C_0, C_1 with probability at least $1-\eta$.

5. COMPRESSIBILITY OF THE ANGULAR SPECTRUM

Let us now analyze the compressibility of coefficients $\{u_n\}$. We present a heuristic argument suggesting that the angular spectrum of the scattered field is sparse for shallow corrugations.

Assuming the validity of the Rayleigh hypothesis we have

$$-u^{\mathrm{inc}}(x,h(x)) = u(x,h(x)) = \sum_{n\in\mathbb{Z}} u_n e^{ik(\alpha_n x+\beta_n h(x))}, \tag{19}$$

or equivalently

$$-e^{-ikh(x)\sin\theta} = \sum_{n\in\mathbb{Z}} u_n e^{ik\beta_n h(x)}e^{inx}.$$

For sufficiently flat and smooth surface h, a nearly normal incidence $\theta \approx \frac{\pi}{2}$ tends to produce a nearly specular diffracted wave [16], and hence $\{u_n\}$ is concentrated at $n=0$. This observation suggests that it may be reasonable to approximate the outgoing wave vector $k\beta_n$ by the negative incoming wave vector $k\beta_0$, or, equivalently, to replace β_n by $\beta_0 = \sin\theta$. With this approximation, we have

$$\sum_{n\in\mathbb{Z}} u_n e^{inx} \approx \frac{-e^{-1kh(x)\sin\theta}}{e^{1k\beta_0 h(x)}} = -1 + 2ikh(x)\beta_0 + \mathcal{O}(k^2|h|^2).$$

Hence, we have

$$u_n \approx v_n \triangleq \begin{cases} -1 & n=0 \\ 2ik\hat{h}_n\beta_0 & n\neq 0, \end{cases} \tag{20}$$

which is sparse by the sparseness assumption on $\{\hat{h}_n\}$ (cf. [6]). Let $Z = \sqrt{m}(v_n e^{ik\beta_n z_0})$. In view of Eq. (8) we have the estimate

$$\|X-X_s\|_1 \approx \|X-Z\|_1 = \sum_{n=-N/2}^{N/2-1}\sqrt{m}|e^{ik\beta_n z_0}||u_n-v_n| \le \sqrt{m}\epsilon_u,$$

where $\epsilon_u \triangleq \sum_{n=-N/2}^{N/2-1}|u_n-v_n|$. Our numerical simulation shows that v_n given in Eq. (20) is indeed an excellent approximation to u_n, at least when the Rayleigh hypothesis is valid.

6. BOUNDARY INTEGRAL FORMULATION

We compute the scattered field $u(x,z_0)$ by the boundary integral method [31,32]. The scattered wave can be represented

by the Brakhage-Werner–type ansatz, i.e., the representation via mixed single-layer (S) and double-layer (K) potentials

$$u = (K - i\eta S)\psi \quad \text{on} \quad \Omega_\Gamma$$

with a mixed layer density ψ for a constant $\eta > 0$, which can be adjusted to improve the condition number of the system. Explicitly, we can write

$$u(x,z) = \int_{-\pi}^{\pi} \left(\frac{\partial}{\partial \nu'} \Phi((x,z),(x',h(x'))) - i\eta \Phi((x,z),(x',h(x'))) \right) \times \psi(x') \cdot \sqrt{1+\dot{h}^2(x')}\,\mathrm{d}x'. \tag{21}$$

Taking the limit $z \to h(x)^+$ and using the properties of single- and double-layer potentials, we obtain the boundary integral equation [31,33]

$$-u^{\mathrm{inc}}(x,h(x)) = \frac{1}{2}\psi(x) + \int_{-\pi}^{\pi} \left(\frac{\partial}{\partial \nu'} \Phi((x,h(x)),(x',h(x'))) - i\eta \Phi((x,h(x)),(x',h(x'))) \right) \times \psi(x') \sqrt{1+\dot{h}^2(x')}\,\mathrm{d}x' \tag{22}$$

(see Appendix A). Note that the integral in Eq. (22) has a weakly singular kernel, and the integral exists as an improper integral since the periodic Green's function

$$\Phi(\boldsymbol{r},\boldsymbol{r}') = \frac{i}{4}\sum_{n\in\mathbb{Z}} e^{2\pi i n k \cos\theta} H_0^{(1)}(k|\boldsymbol{r}-\boldsymbol{r}'-2\pi n(1,0)|), \quad x,x' \in [-\pi,\pi)$$

has the same singularity as $H_0^{(1)}(r) \approx 1 + \frac{2i}{\pi}(\ln\frac{r}{2} + \gamma)$, where $\gamma \approx 0.5772$ is the Euler-Mascheroni constant. Moreover,

$$\frac{\partial}{\partial \nu'} H_0^{(1)}(k|\boldsymbol{r}-\boldsymbol{r}'|) = -kH_1^{(1)}(k|\boldsymbol{r}-\boldsymbol{r}'|)\frac{(\boldsymbol{r}-\boldsymbol{r}')\cdot\nu(\boldsymbol{r}')}{|\boldsymbol{r}-\boldsymbol{r}'|}$$

converges to a finite limit (a curvaturelike term with respect to the boundary) as $\boldsymbol{r} \to \boldsymbol{r}'$ [34], implying the boundedness of $\frac{\partial}{\partial \nu}\Phi$ on Γ.

With ψ solved from Eq. (22) and the Sommerfeld integral representation

$$H_0^{(1)}(k|\boldsymbol{r}|) = \frac{1}{\pi}\int e^{ik(|z|\beta + x\alpha)}\frac{\mathrm{d}\alpha}{\beta}, \tag{23}$$

where

$$\beta = \begin{cases} \sqrt{1-\alpha^2}, & |\alpha| < 1 \\ i\sqrt{\alpha^2-1}, & |\alpha| > 1, \end{cases} \tag{24}$$

we obtain from Eq. (21) the outgoing wave expansion for the scattered field

$$u(x,z) = \sum_{n\in\mathbb{Z}} e^{ik(\alpha_n x + \beta_n z)} \left(\frac{1}{4\pi}\int_{-\pi}^{\pi} e^{-ik(\alpha_n x' + \beta_n h(x'))} g_n(x')\psi(x')\mathrm{d}x' \right), \quad z > h_{\max}, \tag{25}$$

where g_n is the geometric factor

$$g_n(x') = k - k\dot{h}(x')\frac{\alpha_n}{\beta_n} + \frac{\eta}{\beta_n}\sqrt{1+\dot{h}^2(x')}. \tag{26}$$

Comparing Eq. (25) with Eq. (5) we arrive at the expression

$$u_n = \frac{1}{4\pi}\int_{-\pi}^{\pi} e^{-ik(\alpha_n x' + \beta_n h(x'))} g_n(x')\psi(x')\mathrm{d}x' \tag{27}$$

relating the angular spectrum of the scattered field to the mixed layer density ψ.

7. NUMERICAL RESULTS

Equations (22) and (27) suggest the following iterative reconstruction scheme. Given $h^{(m)}$, $m = 1,2,3,\ldots$, first solve for $\psi^{(m)}$ from

$$-u^{\mathrm{inc}}(x,h^{(m)}(x)) = \frac{1}{2}\psi^{(m)}(x) + \int_{-\pi}^{\pi} \left(\frac{\partial}{\partial \nu'} \Phi((x,h^{(m)}(x)),(x',h^{(m)}(x'))) - i\eta \Phi((x,h^{(m)}(x)),(x',h^{(m)}(x'))) \right) \psi^{(m)}(x') \times \sqrt{1+|\dot{h}^{(m)}|^2(x')}\,\mathrm{d}x' \tag{28}$$

and then solve for $h^{(m+1)}$ from

$$u_n = \frac{1}{4\pi}\int_{-\pi}^{\pi} e^{-ik(\alpha_n x' + \beta_n h^{(m)}(x'))} \mathrm{g}_n^{(m+1)}(x')\psi^{(m)}(x')\mathrm{d}x', \qquad n \in \mathbb{Z}, \tag{29}$$

$$g_n^{(m+1)}(x') = k - k\dot{h}^{(m+1)}(x')\frac{\alpha_n}{\beta_n} + \frac{\eta}{\beta_n}\sqrt{1+|\dot{h}^{(m)}|^2(x')}. \tag{30}$$

Note that both Eq. (28) and Eq. (29) are linear equations and can be inverted by Tikhonov regularization.

A natural candidate for the initial guess of the preceding iteration is the one obtained under the Rayleigh hypothesis that the validity of Eq. (25) is extended to the region $z > h(x)$. Specifically, we extend Eq. (25) all the way to the boundary and study the nonlinear equation Eq. (19). Indeed, this alone produces excellent results for shallow corrugations and will be the focus of our numerical experiments.

In our numerical simulations, we set 64 nodes to solve the boundary integral equation, Eq. (22), by the Nyström method, with $\eta = 1$. Figure 2 shows two examples of the computed scattered field. For a profile of multiple Fourier modes, we define $R_a(h) \triangleq \max_n 2|n\hat{h}_n|$ as a metric of surface roughness.

A. Surface Reconstruction

To solve $h(x)$ from Eq. (19), we consider the following three algorithms: the first two are pointwise iterative schemes and the third is a global fitting scheme.

1. Pointwise, fixed-point iteration for $h(x), \forall x \in [-\pi,\pi)$. A fixed-point iteration algorithm was introduced in [14,16] and is described below. The initial condition $h^{[0]}(x)$ is chosen

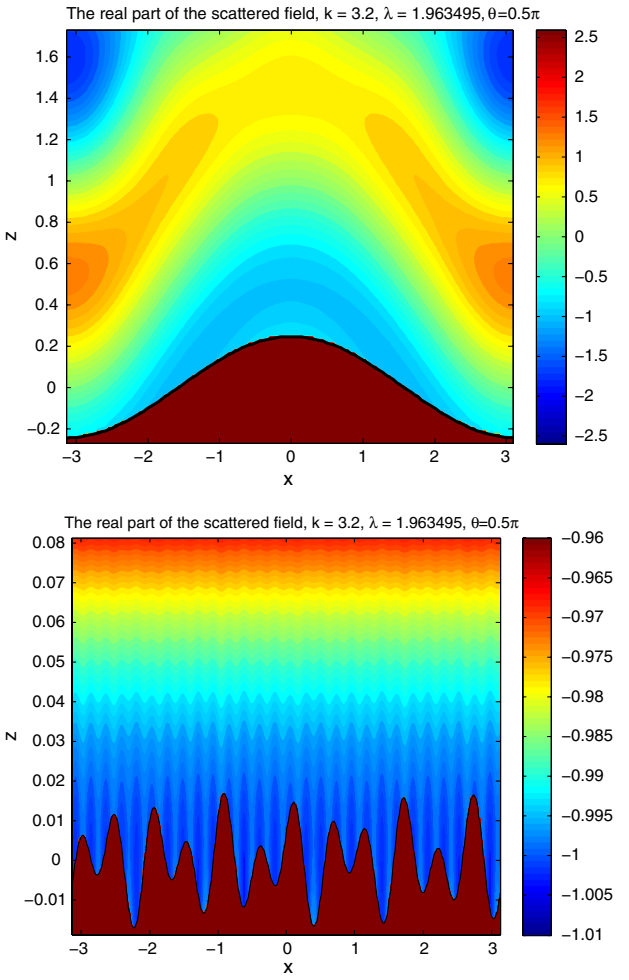

Fig. 2. (Color online) Real part of the scattered field induced by the profile $h(x) = 0.2454\sin(x)$ (top) and the profile $h(x) = 0.01\sin(12x) + 0.007\cos(7x)$ (bottom) with the normal incident plane wave.

in the following way. As explained in Section 5, we substitute β_n by 1 in Eq. (19) and obtain

$$e^{ikh(x)} \cdot \sum_{n\in\mathbb{Z}} u_n e^{ik\alpha_n x} = -e^{ik(x\cos\theta - h(x)\sin\theta)}. \tag{31}$$

We then solve Eq. (31) by the iterative scheme

$$h^{[0]}(x) = \frac{\ln\left(-\sum_{n\in\mathbb{Z}} u_n e^{ik\alpha_n x}\right)}{-2ik}, \tag{32}$$

$$h^{[n+1]}(x) = \frac{\ln\left(-\sum_{n\in\mathbb{Z}} u_n e^{ik(\alpha_n x + (\beta_n - 1)h^{[n]}(x))}\right)}{-2ik} \tag{33}$$

for $n = 1, 2, \ldots$ and all $x \in [-\pi, \pi)$.

2. Newton's method. From Eq. (19), for each $x \in [-\pi, \pi)$ we set

$$e(h; x) = e^{ikx_j\cos\theta} e^{-ikh\sin\theta} + \sum_{n\in\mathbb{Z}} u_n e^{ik\alpha_n x_j} e^{ik\beta_n h}, \tag{34}$$

and find the root $e(h, x) = 0$ by Newton's method

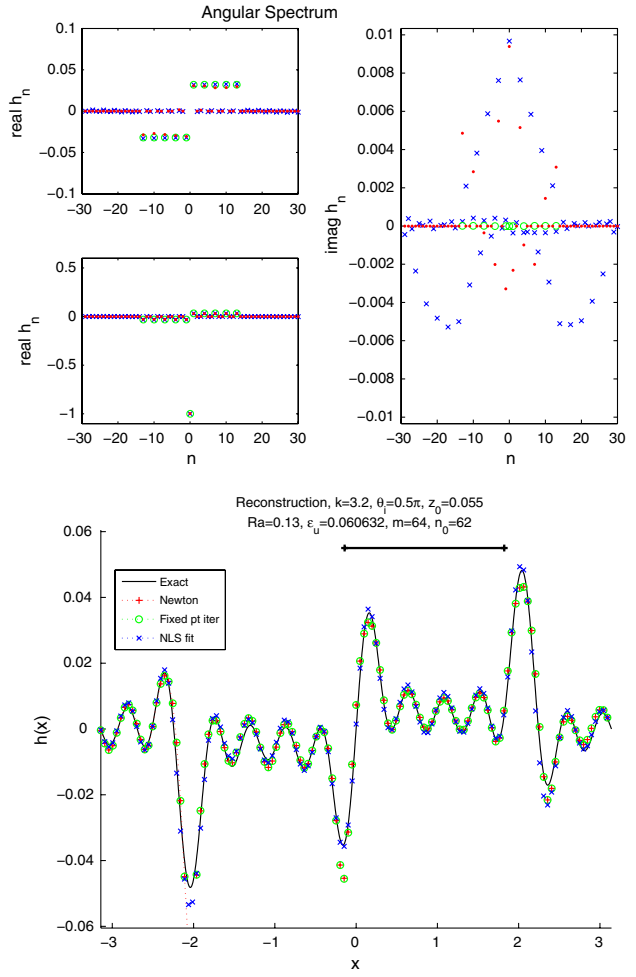

Fig. 3. (Color online) The profile $h(x) = 0.01(\sum_{p=0}^{4} \sin((1+3p)x))$ and the reconstructions (bottom). The top panels show the real part (top left) and the imaginary part (right) of the angular spectrum u_n (blue crosses), the reconstructed angular spectrum $\tilde{u}_n$ (red dots), and the theoretical prediction v_n (green circles).

$$h^{[i+1]} = h^{[i]} - \frac{e(h^{[i]}; x)}{\frac{d}{dh} e(h^{[i]}; x)}$$

with initial value Eq. (32). This method is similar to the one adopted in [8].

3. Nonlinear least squares (NLS) fitting. Let

$$F(\boldsymbol{a}) = \left\| e\left(\sum_n a_n \phi_n(\cdot), \cdot\right)\right\|^2 = \sum_j \left| e\left(\sum_n a_n \phi_n(x_j), x_j\right)\right|^2,$$

where $e(h; x_j)$ is defined in Eq. (34) and $\boldsymbol{a} = (a_1, a_2, \ldots..)$ is the coefficient vector of h with respect to a basis $\{\phi_n\}$, i.e., $h = \sum_n a_n \phi_n$. We then solve the nonlinear least squares problem

$$\min_{\boldsymbol{a}} F(\boldsymbol{a}).$$

For our simulation we use basis functions $\sin(nx)$ and $\cos(nx)$ for $n \in \Pi \subset \mathbb{N}$ with the index set Π corresponding to the significant components $\tilde{u}_n$. We use the MATLAB subroutine lsqnonlin, which is based on the subspace trust region method.

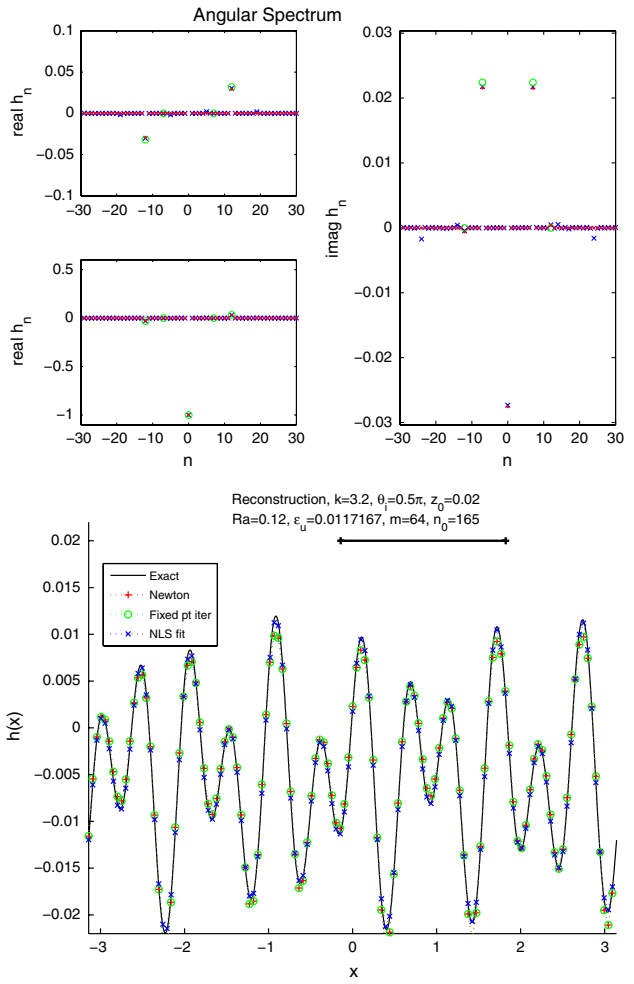

Fig. 4. (Color online) The profile $h(x) = 0.01\sin(12x) + 0.007\cos(7x)$ and the reconstructions (bottom). The labeling is the same as in Fig. 3.

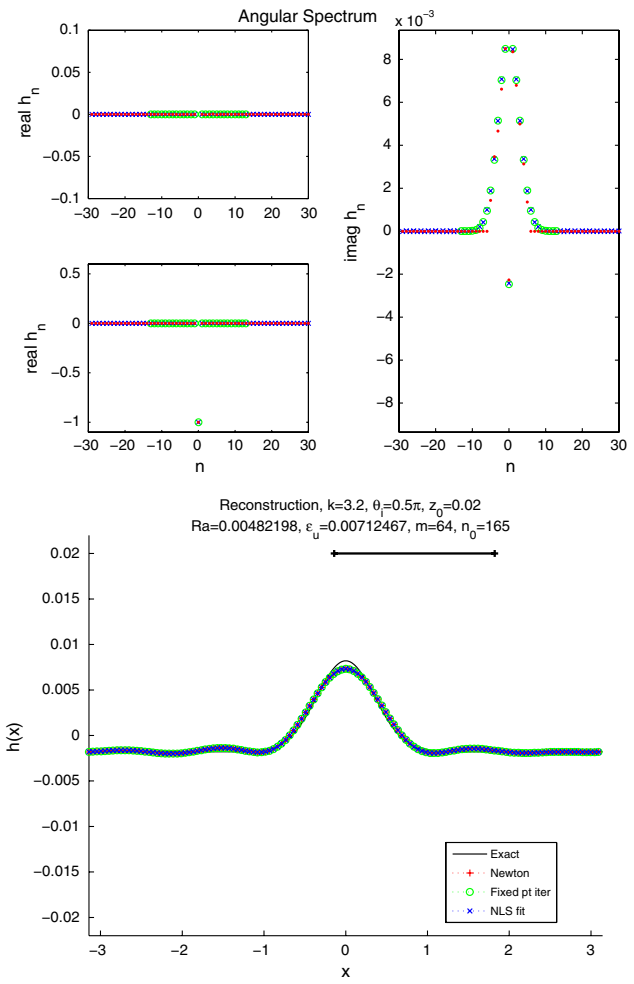

Fig. 5. (Color online) Periodized Gaussian $h(x) = b\left(e^{-(ax)^2} - \frac{\mathrm{erf}(ax)}{\pi\sqrt{\pi}}\right)\cdot\tilde{\chi}_{[-0.9\pi,0.9\pi]}(x)$, $a = 2$, $b = 0.01$ and the reconstructions where $\tilde{\chi}$ is a smoothed indicator function (bottom). The labeling is the same as in Fig. 3.

B. Examples

In our experiments we set $\theta = \frac{\pi}{2}$, with the wave number $k = 3.2$ (i.e., the wavelength $\lambda \approx 1.9635$). After computing the scattered field $u(x_j, z_0)$ for $j = 1, 2, \ldots, 64$, we add 1% noise to the data. The profile functions h are 2π periodic. We set $C_e = \log(25)$ for the cutoff mode [Eq. (17)]. We use the Basis Pursuit solver YALL1 [35] to solve Eq. (10) for vector $\tilde{X}$. We also filter out the components in $\tilde{X}$ below $\tau = 0.1\max_{n\neq 0}|\tilde{X}_n|$ before computing $\tilde{u}_n$ from Eq. (15). The roughness of some of our numerical examples is comparable to those demonstrated in [6,8], which, however, did not study subwavelength modes as we do here.

In Figs. 3–8, the bottom panels show the exact profiles $h(x)$ (black solid line), and the recovered profiles by the three algorithms: Newton's method "Newton," fixed-point iteration "Fixed pt iter," and nonlinear least squares fitting "NLS fit." The length of the black strip on the top of each plot indicates the wavelength, and its height indicates the vertical coordinate z_0 of the sampling points. The top left and right panels show the real (left) and imaginary (right) parts, the angular spectrum u_n (blue crosses), the recovered angular spectrum $\tilde{u}_n$ (red dots), and the theoretical prediction υ_n (green circles). Note the different scales for the real and imaginary parts in Figs. 3 –6 where R_a is relatively small. This is no longer the case in Figs. 7 and 8 for which the Rayleigh hypothesis is known to be false.

Figures 3 and 4 show the results for profiles $h(x)$ with sparse Fourier coefficients. The theoretical prediction υ_n captures well the dominant component $\Re[u_0]$, as does the sparse reconstruction $\tilde{u}_n$ the other significant components of the angular spectrum. For reconstruction (right panels) the nonlinear least squares is the best performer while the pointwise iterative methods undershoot at the peaks and troughs.

For the Gaussian profile (Fig. 5) and subwavelength double peaks (Fig. 6), again υ_n captures well the dominant component $\Re[u_0]$, as does $\tilde{u}_n$ most other significant components of the angular spectrum. The angular spectrum for the latter profile occupies a wider range of modes than the former since the two peaks are sharper than the Gaussian. As a consequence, the reconstruction is more accurate for the former case. For the latter case, all three reconstructions undershoot the peaks and produce fluctuations at the flat part of the profile.

Figures 7 and 8 are the results for simple sinusoids when the Rayleigh hypothesis is known to be invalid ($ab > 0.448$). Like [6,8] these examples do not contain subwavelength modes, and our purpose is to test how violation of the Rayleigh hypothesis degrades the imaging quality.

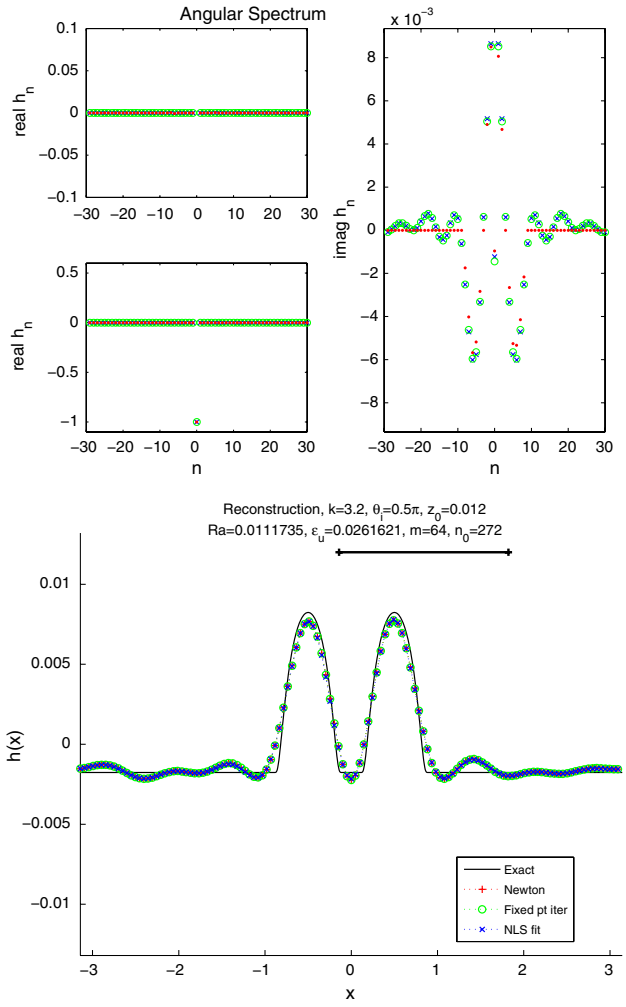

Fig. 6. (Color online) Double subwavelength peaks $h(x) = b(\zeta(a(x-\frac{1}{2})) + \zeta(a(x+\frac{1}{2})))$, $a = 2.5$, $b = 0.01$, $\zeta(x) = \exp\left(1 - \frac{1}{x^2-1}\right)\chi_{(-1,1)}(x) + c_0$ and the reconstructions (bottom). Here the constant c_0 is chosen such that $\hat{\zeta}_0 = 0$. The labeling is the same as in Fig. 3.

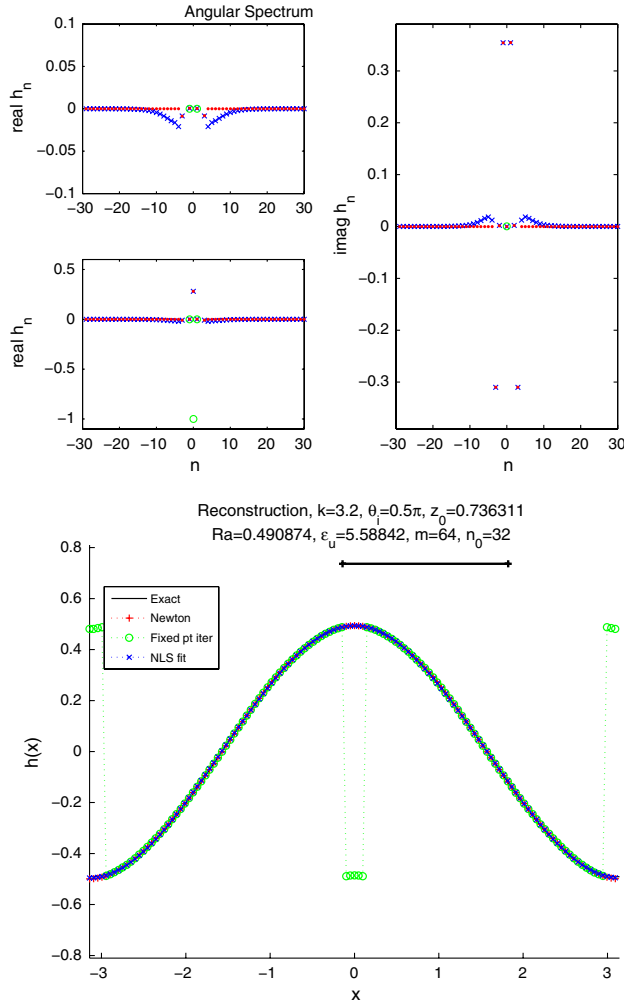

Fig. 7. (Color online) The sinusoidal profile $h(x) = 0.491\cos(x)$ and the reconstructions (bottom). The labeling is the same as in Fig. 3.

The violation of the Rayleigh hypothesis manifests in the broadening of the support of the angular spectrum. Furthermore, the imaginary part of the angular spectrum is an order of magnitude larger than those in Figs. 3–6. As a result, the angular spectrum $\{u_n\}$ is less compressible, and only the dominant modes are recovered by the compressed sensing techniques. In both cases, the simple prediction v_n fails to capture even the dominant components of the angular spectrum.

Nevertheless, the nonlinear least squares fitting provides an accurate reconstruction of the profile in both cases. The Newton iteration converges in Fig. 7 but fails near the peaks and troughs in Fig. 8, while the fixed-point iteration fails to converge near the peaks and troughs in both figures. When ab is further increased (to, e.g., 0.736), all three methods fail to recover the profile.

8. CONCLUSIONS

We have proposed a compressed sensing scheme for near-field imaging of corrugations of relative sparse Fourier components. The scheme employs random sparse measurement of near field to recover the angular spectrum of the scattered field. We have shown heuristically and numerically that under the Rayleigh hypothesis the angular spectrum is indeed sparse or compressible and amenable to compressed sensing techniques.

We have considered three iteration schemes for recovering the surface profile from the angular spectrum. The nonlinear least squares method has the best performance among the three and produces accurate reconstructions even when the Rayleigh hypothesis is known to be invalid.

We have not studied the full iteration scheme Eqs. (28) and (29) beyond the limitation of the Rayleigh hypothesis, which will require nonsparse measurements for the angular spectrum data. We also have neglected the detector tip effect, which may be significant particularly in near-field optics [36]. These issues will be the subject of future investigation.

APPENDIX A: DERIVATION OF BOUNDARY INTEGRAL EQUATION (22)

The term $\frac{1}{2}\psi(x)$ in Eq. (22) arises because of the jump discontinuity for the double-layer potential across the boundary, whereas the single-layer potential is continuous. More specifically, let

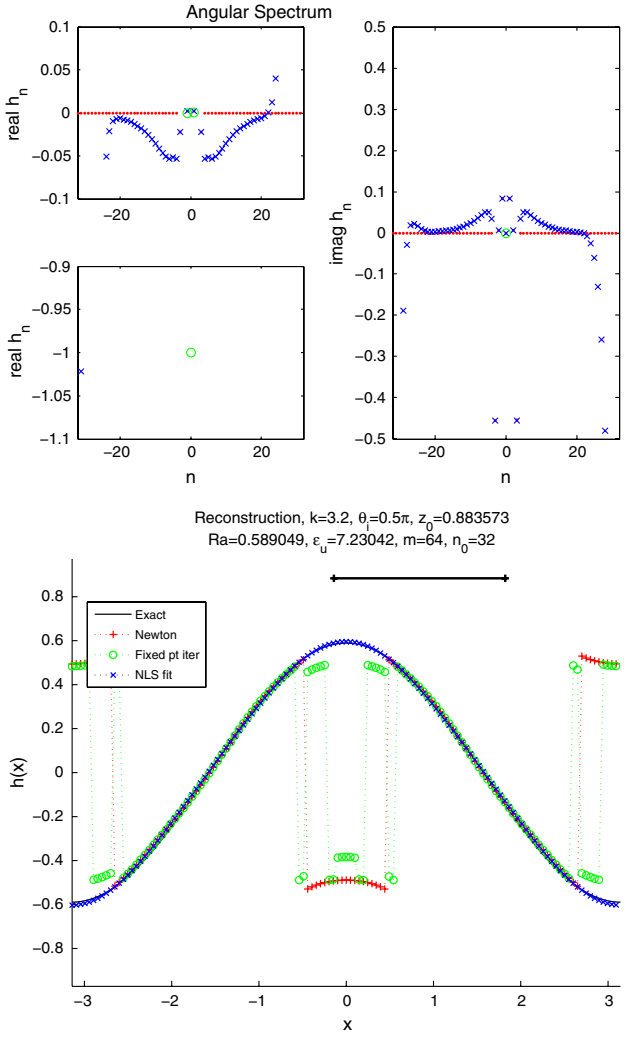

Fig. 8. (Color online) The sinusoidal profile $h(x) = 0.589\cos(x)$ and the reconstructions (bottom). The labeling is the same as in Fig. 3.

$$u_S(\boldsymbol{r}) = \int_\Gamma \Phi(\boldsymbol{r},\boldsymbol{r}')\psi_S(\boldsymbol{r}')\mathrm{d}S(\boldsymbol{r}'), \tag{A1}$$

$$u_D(\boldsymbol{r}) = \int_\Gamma \frac{\partial}{\partial\nu'}\Phi(\boldsymbol{r},\boldsymbol{r}')\psi_D(\boldsymbol{r}')\mathrm{d}S(\boldsymbol{r}') \tag{A2}$$

be the single- and double-layer potentials, respectively, for $\boldsymbol{r} = (x,z) \in \mathbb{R}^2\backslash\Gamma$. Furthermore, we denote $\boldsymbol{r}^\pm = \boldsymbol{r}_0 \pm \rho\nu(\boldsymbol{r}_0)$ for some small $\rho > 0$ and $\boldsymbol{r}_0 \in \Gamma$ (assuming that the boundary is of class C^2 so the representation of $\boldsymbol{r}^\pm$ is unique for $\boldsymbol{r}^\pm$ near the boundary). Clearly

$$\lim_{\rho\to 0} u_S(\boldsymbol{r}^+) = \lim_{\rho\to 0} u_S(\boldsymbol{r}^-) = u_S(\boldsymbol{r}_0).$$

On the other hand, write

$$u_D(\boldsymbol{r}^+) = \psi_D(\boldsymbol{r}_0)\int_\Gamma \frac{\partial}{\partial\nu'}\Phi_0(\boldsymbol{r}^+,\boldsymbol{r}')\mathrm{d}S(\boldsymbol{r}') + v(\boldsymbol{r}^+), \tag{A3}$$

$$u_D(\boldsymbol{r}^-) = \psi_D(\boldsymbol{r}_0)\int_\Gamma \frac{\partial}{\partial\nu'}\Phi_0(\boldsymbol{r}^-,\boldsymbol{r}')\mathrm{d}S(\boldsymbol{r}') + v(\boldsymbol{r}^-) \tag{A4}$$

so that

$$v(\boldsymbol{r}^\pm) = \int_\Gamma \frac{\partial}{\partial\nu'}\Phi(\boldsymbol{r}^\pm,\boldsymbol{r}')(\psi_D(\boldsymbol{r}') - \psi_D(\boldsymbol{r}_0))\mathrm{d}S(\boldsymbol{r}') + \psi_D(\boldsymbol{r}_0) \times \int_\Gamma \left(\frac{\partial}{\partial\nu'}\Phi(\boldsymbol{r}^\pm,\boldsymbol{r}') - \frac{\partial}{\partial\nu'}\Phi_0(\boldsymbol{r}^\pm,\boldsymbol{r}')\right)\mathrm{d}S(\boldsymbol{r}'), \tag{A5}$$

where Φ_0 is Green's function for the Laplace equation. It is easy to see that integral Eq. (A5) is continuous in the neighborhood of $\rho = 0$.

The jump condition

$$\lim_{\rho\to 0}(u_D(\boldsymbol{r}^+) - u_D(\boldsymbol{r}^-)) = \psi_D(\boldsymbol{r}_0)$$

now follows from the calculation

$$\int_\Gamma \frac{\partial}{\partial\nu'}\Phi_0(\boldsymbol{r}^\pm,\boldsymbol{r}')\mathrm{d}S(\boldsymbol{r}') = \frac{1}{2}\int_{\partial B_\rho(\boldsymbol{r}_0)} \frac{\partial}{\partial\nu'}\Phi_0(\boldsymbol{r}^\pm,\boldsymbol{r}')\mathrm{d}S(\boldsymbol{r}')$$

$$= \frac{1}{4\pi\rho}\int_{\partial B_\rho(\boldsymbol{r}_0)} \pm 1\mathrm{d}S(\boldsymbol{r}') \to \pm\frac{1}{2}, \qquad \rho \to 0$$

by applying the divergence theorem, integrating over the circle $B_\rho(\boldsymbol{r}_0)$ of radius ρ, and shrinking radius ρ to 0.

ACKNOWLEDGMENT

The research was supported in part by NSF Grant DMS 0908535.

REFERENCES

1. P. Beckmann, "Scattering of light by rough surfaces." Prog. Opt. **6**, 53–69 (1967).
2. F. B. Bass and I. M. Fuks, *Wave Scattering from Statistically Rough Surfaces* (Pergamon, 1980).
3. O. Ivanyshyn and T. Johanson, "Nonlinear integral equation methods for the reconstruction of an acoustically sound soft obstacle," J. Integral Equ. Appl. **19**, 289–308 (2007).
4. A. Schatzberg and A. J. Devaney, "Rough surface inverse scattering within the Rytov approximation," J. Opt. Soc. Am. A **10**, 942–950 (1993).
5. J. L. Uretsky, "The scattering of plane waves from periodic surfaces," Ann. Phys. **33**, 400–427 (1965).
6. R. J. Wombell and J. A. DeSanto, "The reconstruction of shallow rough-surface profiles from scattered field data," Inverse Probl. **7**, L7–L12 (1991).
7. R. J. Wombell and J. A. DeSanto, "Reconstruction of rough-surface profiles with Kirchhoff approximation," J. Opt. Soc. Am. A **8**, 1892–1897 (1991).
8. A. Yapar, O. Ozdemir, H. Sahinturk, and I. Akduman, "A Newton method for the reconstruction of perfectly conducting slightly rough surface profiles," IEEE Trans. Antennas Propag. **54**, 275–279 (2006).
9. E. A. Ash and G. Nicholls, "Super-resolution aperture scanning microscope," Nature **237**, 510–512 (1972).
10. B. Hecht, B. Sick, U. P. Wild, V. Deckert, R. Zenobi, O. J. F. Martin, and D. W. Pohl, "Scanning near-field optical microscopy with aperture probes: fundamentals and applications," J. Chem. Phys. **112**, 7761–7774 (2000).
11. A. Lewis, M. Isaacson, A. Harootunian, and A. Murray, "Development of a 500 Å spatial resolution light microscope. I. Light is efficiently transmitted through $\lambda/16$ diameter apertures," Ultramicroscopy **13**, 227–231 (1984).

12. D. W. Pohl, W. Denk, and M. Lanz, "Optical stethoscopy: image recording with resolution $\lambda/20$," Appl. Phys. Lett. **44**, 651 (1984).
13. B. T. Khuri-Yakub, S. Akamine, B. Hadimioglu, H. Yamada, and C. F. Quate, "Near field acoustic microscopy," Proc. SPIE **1556**, 30–39 (1991).
14. N. Garcia and M. Nieto-Vesperinas, "Near-field optics inverse-scattering reconstruction of reflective surfaces," Opt. Lett. **18**, 2090–2092 (1993).
15. M. Nieto-Vesperinas and N. Garcia, "A detailed study of the scattering of scalar waves from random rough surfaces," Opt. Acta **28**, 1651–1672 (1981).
16. K. H. Riedera, N. Garcia, and V. Celli, "An effective procedure to determine corrugation functions from atomic beam-diffraction intensities," Surf. Sci. **108**, 169–180 (1981).
17. A. Fannjiang, "Compressive imaging of subwavelength structures," J. Imaging Sci. **2**, 1277–1291 (2009).
18. B. Deutsch, R. Hillenbrand, and L. Novotny, "Near-field amplitude and phase recovery using phase-shifting interferometry," Opt. Express **16**, 494–501 (2008).
19. E. J. Candès and T. Tao, "Near-optimal signal recovery from random projections: universal encoding strategies," IEEE Trans. Inf. Theory **52**, 5406–5425 (2006).
20. D. L. Donoho, "Compressed sensing," IEEE Trans. Inf. Theory **52**, 1289–1306 (2006).
21. A. Kirsch, "Diffraction by periodic structures," in *Inverse Problems in Mathematical Physics* (Springer-Verlag, 1993), Vol. **422**, pp. 87–102.
22. T. Arens and T. Hohage, "On radiation conditions for rough surface scattering problems," IMA J. Appl. Math. **70**, 839–847 (2005).
23. G. Derveaux, G. Papanicolaou, and C. Tsogka, "Resolution and denoising in near-field imaging," Inverse Probl. **22**, 1437–1456 (2006).
24. R. F Millar, "On the Rayleigh assumption in scattering by a periodic surface," Math. Proc. Cambridge Philos. Soc. **65**, 773–791 (1969).
25. R. F Millar, "On the Rayleigh assumption in scattering by a periodic surface II," Math. Proc. Cambridge Philos. Soc. **69**, 217–225 (1971).
26. J. B Keller, "Singularities and Rayleigh's hypothesis for diffraction gratings," J. Opt. Soc. Am. A **17**, 456–457 (2000).
27. T. Arens, S. N. Chandler-Wilde, and J. A. DeSanto, "On integral equation and least squares methods for scattering by diffraction gratings," Commun. Comput. Phys. **1**, 1010–1042 (2006).
28. S. S. Chen, D. L. Donoho, and M. A. Saunders, "Atomic decomposition by basis pursuit," SIAM Rev. **43**, 129–159 (2001).
29. H. Rauhut, "Stability results for random sampling of sparse trigonometric polynomials," IEEE Trans. Inf. Theory **54**, 5661–5670 (2008).
30. E. J. Candès, "The restricted isometry property and its implications for compressed sensing," C. R. Acad. Sci. **346**, 589–592 (2008).
31. J. DeSanto, G. Erdmann, W. Hereman, and M. Misra, "Theoretical and computational aspects of scattering from rough surfaces: one-dimensional perfectly reflecting surfaces," Waves Random Media **8**, 385–414 (1998).
32. A. Meier, T. Arens, S. N. Chandler-Wilde, and A. Kirsch, "A Nyström method for a class of integral equations on the real line with applications to scattering by diffraction gratings and rough surfaces," J. Integral Equ. Appl. **12**, 281–321 (2000).
33. D. Colton and R. Kress, *Integral Equation Methods in Scattering Theory* (Wiley, 1983).
34. D. Colton and R. Kress, *Inverse Acoustic and Electromagnetic Scattering Theory*, 2nd ed. (Springer, 1998).
35. J. Yang and Y. Zhang, "Alternating direction algorithms for L1 problems in compressive sensing," TR09-37 (CAAM, Rice University , 2010).
36. J. Sun, P. S. Carney, and J. C. Schotland, "Strong tip effects in near-field scanning optical tomography," J. Appl. Phys. **102**, 103013 (2007).